

**Manchester
Metropolitan
University**

Stacy, J and Regmi, YN and Leonard, B and Fan, M (2017) The recent progress and future of oxygen reduction reaction catalysis: A review. *Renewable and Sustainable Energy Reviews*, 69. pp. 401-414. ISSN 1364-0321

Downloaded from: <http://e-space.mmu.ac.uk/624897/>

Version: Accepted Version

Publisher: Elsevier

DOI: <https://doi.org/10.1016/j.rser.2016.09.135>

Please cite the published version

<https://e-space.mmu.ac.uk>

The Recent Progress and Future of Oxygen Reduction Reaction Catalysis: A Review

John Stacy^a, Yagya N Regmi^b, Brian Leonard^b, Maohong Fan^{a,c}

^a*Department of Chemical Engineering, University of Wyoming, Laramie, Wyoming, 82017, USA*

^b*Department of Chemistry, University of Wyoming, Laramie, Wyoming, 82071, USA*

^c*School of Energy Resources, University of Wyoming, Laramie, Wyoming, 82071, USA*

* Corresponding author: Maohong Fan; mfan@uwyo.edu

Keywords: oxygen reduction reaction, d-band shift, Pt-alloys, precious-metal-free catalysts, metal-free catalysts

Abstract

Proton Exchange Membrane Fuel Cell (PEMFC) technology is an exciting alternative energy prospect, especially in the field of transportation. PEMFCs are three times as efficient as internal combustion (IC) engines and emit only water as a byproduct. The latter point is especially important in a day and age when climate change is upon us. However, platinum required to catalyze the sluggish oxygen reduction reaction (ORR) which takes place on the cathode of the PEMFC has rendered fuel cell automobiles economically unviable until now. Therefore, the pursuit of an inexpensive replacement for platinum has become an active research area. This review covers the promising progress made in this field since 2011. Some of the more promising catalysts reviewed include alloys such as Pt/Pd nanotubes which outperform their platinum counterpart by nine fold and a Pt/Ni alloy which improves upon Pt activity by 16 times.

Platinum-free catalysts such as iron carbide and modified graphene which rival Pt activity are also reviewed.

Table of Contents

1. Introduction	3
1.1 The Reaction	4
1.2 Optimizing ORR catalysts.....	7
2. Platinum Alloys and Platinum-Free Catalysts.....	9
2.1 Platinum Alloys.....	9
2.1.1 Platinum-Noble Metal Alloys.....	10
2.1.2 Platinum-Transition Metal Alloys	15
2.2 Platinum-Free Catalysts	19
2.2.1 Platinum-Free Transition Metal Based Catalysts	19
2.2.2 Metal-Free Catalysts	24
3. Conclusion.....	Error! Bookmark not defined.

1. Introduction

Internal combustion (IC) engine based vehicles have served people for over 150 years. Obviously, their contributions to the progress of modern civilization can never be overestimated. However, their detrimental impacts on the environment should not be underestimated either. IC engines are inefficient (15%), and emit harmful pollutants including CO₂, around which much controversy has risen [1-6]. Therefore, it is essential that alternative methods for fueling transportation are pursued. Among these alternatives is proton exchange membrane fuel cell (PEMFC) technology. PEMFC vehicles boast much higher energy efficiencies (50-60%) than IC engines and zero carbon emissions [7].

Many obstacles stand in the way of the commercialization of PEMFC vehicles such as hydrogen production and fueling station infrastructure [8]. However, the high cost of PEMFC vehicles is what keeps them from becoming realistic competitors to IC automobiles. The costliest component of the PEMFC is platinum which catalyzes both the anodic and cathodic reaction. Platinum catalyzes the oxidation of H₂ into protons and electrons on the anode, but the overpotential for this reaction is relatively low necessitating correspondingly low loadings of platinum [9]. However, a much larger loading of platinum is required on the cathode in order to catalyze the sluggish and rate limiting oxygen reduction reaction (ORR) [10-12].

Obviously, the cost of this platinum catalyst is the main hindrance to mass production of PEMFC vehicles. Indeed, platinum loadings in PEMFCs need to be cut by a factor of ten in order to make PEMFC automobiles economically competitive with their IC counterparts [13, 14]. In addition, the limited supply of the precious metal (PM) is not

abundant enough to sustain global mass production of fuel cell cars without cost-effective recycling methods [15].

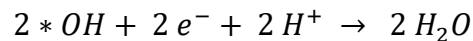
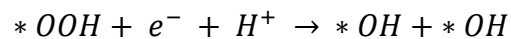
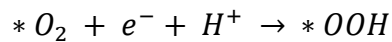
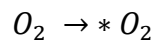
Therefore, a number of studies have been conducted to develop new ORR catalysts which can overcome the abovementioned challenges associated with the use of platinum catalysts. These studies have been focused on two areas: alloying the precious metal with another metal in order to increase the mass activity with respect to platinum ($A \text{ mg}^{-1}\text{-Pt}$) and, eliminating the need for platinum by producing non-precious metal catalysts that can match platinum in catalytic activity. This review will cover the advances in these fields that have been made in the last five years.

1.1 The Reaction

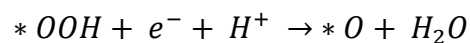
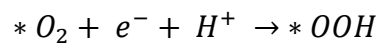
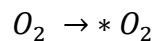
ORR can take place via two pathways. The first, commonly referred to as partial reduction, involves a two electron pathway resulting in the production of adsorbed hydrogen peroxide. Full reduction follows a more efficient four electron pathway which does not involve the production of H_2O_2 [16-18]. Due to the improved efficiency of full reduction as well as the relatively high reactivity of hydrogen peroxide compared to the stability of water, full reduction is the pathway that is sought after when choosing a catalyst for the ORR [19]. For partial reduction to take place, O_2 is first adsorbed on to the catalyst surface. Then, two hydrogen additions take place resulting in an adsorbed H_2O_2 molecule. The hydrogen peroxide product can then undergo further reduction to produce two water molecules, or it can simply dissociate resulting in a free H_2O_2 molecule [18, 20]. Full reduction is a dissociative adsorption process which begins with the adsorption of O_2 on the catalyst surface. Following O_2 adsorption, the first electron transfer in the form of hydrogen addition takes place resulting in $^*\text{OOH}$. This is followed by the second electron transfer, again in the form of hydrogen addition. Depending on

whether this second hydrogen addition takes place at the oxygen molecule adsorbed to the catalyst or if it takes place at the oxygen already bound to the hydrogen determines how the reaction moves forward. If the second hydrogen addition takes place at the oxygen adsorbed to the catalyst (mechanism 1), it results in two adsorbed OH groups. Subsequent electron transfers in the form of hydrogen addition take place at each *OH group resulting in the production of two water molecules. If the second hydrogen addition takes place at the oxygen already bound to the first hydrogen (mechanism 2), this results in desorption of a water molecule and an adsorbed O atom. Two electron transfers in the form of hydrogen addition to the *O follow resulting in desorption of a second water molecule. DFT simulations of the two pathways show that mechanism 1 is thermodynamically favored, and it is therefore the more realistic method [18, 20-23].

Mechanism 1



Mechanism 2



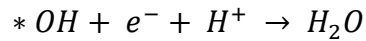
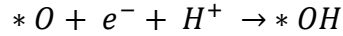


Fig. 1. Mechanism schematics based on the work of Zhang et al. [24] of (a) full reduction and (b) partial reduction of oxygen

1.2 Sustainability

Although the operation of the fuel cell itself produces no harmful emissions, the production of the high purity hydrogen fuel does. This hydrogen production is carried out in a variety of ways, all with their own advantages and disadvantages.

Most of the hydrogen production technologies utilize natural gas as a feed stock. Hydrogen is produced from natural gas via steam methane reforming during which methane is reacted with steam to produce CO and H₂. This is followed by the water gas shift reaction which, in the presence of steam, converts the remaining CO to CO₂ and more H₂. Although this process does produce CO₂, it emits none of the harmful NO_x which are emitted by internal combustion engines.

18% of the hydrogen produced around the world is made using coal as a feed stock. This involves the gasification of coal to synthesis gas, mostly CO and H₂. The CO is reacted with steam in the water gas shift reaction to produce more hydrogen and CO₂. Again, hydrogen production via coal results in the production of CO₂ along with other pollutants associated with coal. However, an argument can be made that hydrogen production using coal is more sustainable than using natural gas since coal resources are far more abundant than those of natural gas.

The most environmentally friendly hydrogen production method is electrolysis, which splits water into hydrogen and oxygen gas using electric current. The sustainability of hydrogen production via electrolysis depends on the electricity source. If renewable energy sources such as solar or wind are used to power electrolysis, PEMFCs can truly be zero emission vehicles.

Regardless of hydrogen production method, the efficiency of PEMFCs makes them sustainable and attractive. These efficiencies translate to 60 mpg on an mpg basis, far outperforming their IC counterparts. So, whatever the feedstock, these efficiencies mean that that stock will last longer [25].

1.3 Optimizing ORR catalysts

Density functional theory (DFT) calculations indicate that the binding energy between oxygen intermediates and the catalyst surface is related to catalytic efficiency for ORR [17, 26]. The Sabatier principle is the idea that a reactant must bind strongly enough to the catalyst for the reaction to take place, but weakly enough that the product will dissociate and the catalyst surface will not be poisoned by either the reactant or intermediates [27-30]. So, in this case the oxygen species must bind tightly enough to the catalyst that the reaction can take place on the surface, but not so tightly that oxygen intermediates poison the catalyst. Based on both theoretical calculations and experimental data, “volcano plots,” like the one seen in figure 2, can be constructed comparing catalytic activity to oxygen binding energy (ΔE_O) [23]. These plots can then be used to find the optimal ΔE_O for an ORR catalyst.

Fig. 2. Volcano plot showing relationship between oxygen binding energy and maximal activity calculated using Sabatier Analysis. Reproduced with permission from Nørskov, J.K., et al., *Origin of the overpotential for oxygen reduction at a fuel-cell cathode*. The Journal of Physical Chemistry B, 2004. **108**(46): p. 17886-17892. Copyright 2004 American Chemical Society. [23, 29]

Among the catalysts under consideration in figure 2, Pt catalysts occupy the most optimal position. However, Pt is not at the peak of the volcano. Therefore, there is room for improvement when designing an ORR catalyst. One method to change adsorption energies of oxygen intermediates is adjusting the center of the d-band, or conductive band, of the catalyst. The d-band acts as a descriptor of the electronic properties of the solid, and it has been shown to correlate with adsorption energies [31]. Bimetallic catalysts, specifically core shell arrangements, have been shown to shift the d-band center relative to bulk metals [32, 33]. In section 2.1.1, Kuttiyiel et al. use this d-band/ ΔE_{O} correlation along with a Sabatier style volcano plot in order to optimize the d-band center for their catalyst [34]. Another method for changing the electronics of a catalyst is tuning the predominant facets that are present on the surface [35]. Each crystal plane possesses a specific surface energy, and therefore different binding energies to reactants and different ORR activities [36]. Indeed, Stamenkovic et al. have shown that a Pt (111) single crystal catalyst displays an ORR activity ~ 10 times larger than state of the art Pt/C catalysts with a mixture of facets on the catalyst surface [13]. Furthermore, applying a Pt monolayer on a Pd or Pd₃Co nano-particle core results in a strain on this (111) face increasing the rate of ORR even more [36].

Innovation in the field of reaction modeling has allowed for computational studies to be carried out via DFT which allow for some optimization prior to experimental exploration. Greeley and Norskov have established a starting point for many (nearly 750) binary Pt alloys by determining theoretically not only the potential of a material for ORR activity, but also how the material will stand up to the harsh environment of PEMFCs [37].

Morphology is also an important factor when optimizing a catalyst. Of course, as particle size decreases the surface area to volume ratio increases. This gives rise to more sites upon which catalysis can take place. So, nanoparticles are optimal for any heterogeneous catalytic process, including ORR. However, the shape of the nanoparticles is also important. Morphology with a high number of corner or edge sites can give rise to further improvement in activity, as will be discussed in section 2.1.1 [38].

2. Platinum Alloys and Platinum-Free Catalysts

2.1 Platinum Alloys

Platinum alloys have two distinct advantages over pure Pt catalysts: i.) interactions between the two metals give rise to modifications to the electronic properties of the material, some of which result in higher ORR activity [32-34] ii.) incorporation of another metal leads to a decreased platinum loading while at least maintaining high catalytic activity and therefore a higher mass activity ($A \text{ mg}^{-1}\text{-Pt}$) [39-41]. This effect is amplified if the alloying metal can be manipulated to inhabit the core of the particle

leaving the active platinum on the surface. The following materials have advanced the field of ORR catalysis by embracing one or both of the advantages mentioned above.

2.1.1 Platinum-Noble Metal Alloys

Noble metals are known for their resistance to oxidation and robustness in acidic environments [42, 43]. Therefore, they are good candidates as additives to platinum catalysts that suffer from relatively poor stability in PEMFCs due to Ostwald ripening [44].

Zhang et al. have established a one-pot solution synthesis to produce a nanodendritic morphology for a platinum-on-iridium catalyst. This synthesis resulted in a very even dispersion of ~15 nm particles as seen in figure 3 a with a 2:1 Ir:Pt molar ratio. Elemental line profiles confirm the Ir/Pt core/shell composition. The nanodendritic nature of these particles gave rise to an increase in electrochemical surface area (ECSA). Zhang et al. site this, along with the interaction between the iridium core and the platinum shell as the reasons behind the impressive ORR activity exhibited by this catalyst when compared to a 1:1 molar mixture of iridium and platinum black. Increased corner and edge sites which are present in abundance in nanodendritic morphology may also play a role [45]. As seen in figure 3 b, rotating disk electrode (RDE) studies show that the Pt/Ir catalyst drastically outperformed the Pt black/Ir mixture with a mass activity of ~0.12 A mg⁻¹-Pt compared to ~0.06 A mg⁻¹-Pt at 0.8 V vs. a reversible hydrogen electrode (RHE) in a 0.5 M H₂SO₄ solution [46].

Fig. 3. (a) TEM image of Pt/Ir nanodendrites (b) linear sweep voltammogram comparing ORR activity of Pt/Ir nanodendrites and Ir-Pt mixture. Reproduced from *Electrochemistry Communications*, 22, Zhang, G., et al., *One-pot synthesis of Ir@Pt nanodendrites as highly active bifunctional electrocatalysts for oxygen reduction and oxygen evolution in acidic medium*. p. 145-148 with permission from Elsevier. [46]

Yeo et al. used gold seed mediated growth to prepare Pt/Au nanodendrites. Synthesis without gold seeds resulted in relatively large particles of Pt (~40 nm in diameter), but the gold seed mediated synthesis resulted in monodispersed (~15 nm) nanodendrites. These catalysts outperformed Pt black in RDE studies by a factor of 3, displaying a mass activity of ~0.3 A mg⁻¹-Pt at 0.85 V vs. RHE in 0.1 M HClO₄. These values were calculated based on figure 4 using a catalyst loading of 15.3 μg_{Pt} cm⁻² for each catalyst. Inductively coupled plasma atomic-emission spectroscopy (ICP-AES) measurements showed only a 1% loading of gold in the Pt/Au nanodendrites. The negligible amount of gold present in the particles along with the fact that these catalysts outperformed Pt/Au hybrid nanospheres in RDE testing implies that the improved activity seen is likely due to the increased corner and edge sites as well as the high ECSA that arise in nanodendritic morphology rather than from an interaction between the relatively small amount of gold and the platinum in the particles [38, 45, 47]

Fig. 4. Linear sweep voltammogram comparing Pt/Au nanodendrites and platinum black [38]

Karan et al. reduced metal chlorides under hydrogen gas to produce IrRe nanoparticles (NPs). These NPs were then coated with either a monolayer of Pt, or a monolayer of Pt on a monolayer of Pd via Galvanic displacement resulting in Pt/IrRe and Pt/Pd/IrRe catalysts respectively with diameters of ~ 4 nm. Both of these catalysts outperformed a conventional Pt/C catalyst in RDE studies. The Pt/IrRe exhibited a mass activity of ~ 0.4 A mg^{-1} -Pt at 0.9 V vs. RHE in 0.1 M HClO_4 compared to ~ 0.6 A mg^{-1} -Pt exhibited by Pt/Pd/IrRe and ~ 0.2 A mg^{-1} -Pt exhibited by Pt/C. In order to explain the improved activity exhibited by the Pt/Pd/IrRe and Pt/IrRe catalysts DFT calculations of catalyst-OH binding energies were carried out and plotted against experimental current densities resulting in the volcano plot seen in figure 5. DFT calculations were possible only for stable bulk phase IrRe mole ratios ruling out the Ir_2Re_1 core configuration that showed the highest experimental ORR activity. However, this study confirms that varying the Ir:Re composition changes the catalyst-OH binding energy therefore changing the ORR activity [48].

Fig. 5. Volcano plot displaying calculated OH binding energy vs. experimentally measured current density. Adapted with permission from Karan, H.I., et al., *Catalytic activity of platinum monolayer on iridium and rhenium alloy nanoparticles for the oxygen reduction reaction*. ACS Catalysis, 2012. 2(5): p. 817-824. Copyright 2012 American Chemical Society [48]

Shao et al. experimented with depositing a platinum monolayer on gold nanoparticles. The resulting catalysts were monodispersed (~ 3 nm) particles. These Pt/Au NPs showed

further improvement in terms of ORR activity displaying a mass activity of $\sim 1.2 \text{ A mg}^{-1}\text{-Pt}$ compared to $\sim 0.2 \text{ A mg}^{-1}\text{-Pt}$ shown by Pt/C at 0.9 V vs. RHE in 0.1 M HClO₄. The particle size of the Pt/C catalysts were $\sim 2.8 \text{ nm}$, nearly identical to that of the Pt/Au NPs thus ruling out the possibility of increased catalytic activity due to increased surface area. The experimental trend is in contradiction to DFT calculations found in the literature which indicate that large tensile strain at the surface of single crystal Pt/Au should create a stronger than optimal OH binding energy slowing down the ORR [24]. However, Shao et al. performed DFT calculations utilizing a larger catalyst model (nanoparticles ranging from 1.5 to 5 nm), and these calculations show that a compressive strain arises in the surface of these catalysts. The compressive strain is thought to be responsible for the shift in the d-band and the increased ORR activity [49].

Kuttiyiel et al. prepared a catalyst consisting of an IrNi alloy core coated with first a monolayer of iridium and then a monolayer of platinum. The resulting catalysts were $\sim 5 \text{ nm}$ spheres. Again, electrochemical tests were performed for a comparison against the state of the art Pt/C catalyst. The Pt/Ir/IrNi catalysts exhibited a mass activity of $\sim 1.4 \text{ A mg}^{-1}\text{-Pt}$ compared to $\sim 0.2 \text{ A mg}^{-1}\text{-Pt}$ exhibited by the Pt/C at $\sim 0.9 \text{ V}$ vs. RHE in 0.1 M HClO₄. Previous DFT studies indicate that pairing a Pt shell with a pure Ir core results in OH adsorbing too strongly on the catalyst surface effectively poisoning the catalyst [50]. However, as seen in Figure 6 b, the addition of nickel in the core shifts the d-band center to a slightly more positive value from $\sim -2.25 \text{ eV}$ to $\sim -2.1 \text{ eV}$. This shift weakens the catalyst-OH bond when compared to Pt/Ir models and strengthens the catalyst-OH bond slightly compared to that of Pt catalysts. The result is a more optimal catalyst-OH

binding energy and an improvement in ORR activity. The optimization of specific activity vs. binding energy is made evident by the volcano plot shown in Figure 6 a [34].

Fig. 6. (a) plot comparing d-band center and oxygen binding energy (b) plot of current density vs. oxygen binding energy. Reproduced from [34] with permission of The Royal Society of Chemistry.

Alia et al. have developed a strategy to produce platinum-coated palladium nanotubes via a partial galvanic displacement of Pd nanotubes. Three catalysts were synthesized with platinum coatings 1.1, 1.7 and 2.2 atoms thick corresponding to Pt weight percentages of 9, 14, and 18 (PtPd9, PtPd14, and PtPd18 respectively). The resulting Pt/Pd tubes had wall thicknesses and outer diameters of 6 and 60 nm respectively as seen in figure 7. ORR polarization curves were recorded to compare these catalysts to a state of the art Pt/C catalyst. The PtPd9 exhibited the highest mass activity at $\sim 1.8 \text{ A mg}^{-1}\text{-Pt}$ compared to $\sim 1.1 \text{ A mg}^{-1}\text{-Pt}$ for PtPd14 and $\sim 0.9 \text{ A mg}^{-1}\text{-Pt}$ for PtPd18 (all at 0.9 V vs. RHE in 0.1 M HClO₄). All three of the PtPd catalysts outperformed the Pt/C catalyst which exhibited a mass activity of just $\sim 0.2 \text{ A mg}^{-1}\text{-Pt}$. Electrochemical surface area studies showed that the PtPd nanotubes possessed a surface area of $\sim 16 \text{ m}^2 \text{ g}^{-1}$ compared to the $\sim 64 \text{ m}^2 \text{ g}^{-1}$ shown by the Pt/C catalyst. Therefore, it can be assumed that the improved catalytic activity seen by the PtPd catalysts is due to the metal-metal interaction, and not increased surface area [51].

Fig. 7. (a) TEM image of PtPd14 (b) SEM image of PtPd14. Reprinted with permission from Alia, S.M., et al., *Platinum-coated palladium nanotubes as oxygen reduction reaction electrocatalysts*. ACS Catalysis, 2012. **2**(5): p. 858-863. Copyright 2012 American Chemical Society. [51]

Fig. 8. Comparison of power densities for Pt/PM alloy catalysts [34, 38, 46, 48, 49, 51]

Figure 8 displays power densities (the product of current density and cell potential vs. RHE), rather than current densities, in order to normalize for reported current densities at different cell potentials. All of these catalysts were tested in 0.1 M HClO₄ with the exception of the Pt/Ir nanodendrites produced by Zhang et al. which were tested in 0.5 M H₂SO₄ [46]. This difference in electrolyte can explain the disparity in Pt performance seen in these studies. All of the abovementioned alloy or core-shell catalysts outperform their platinum counterparts under identical conditions, and the use of these alloys means less platinum is required for each catalyst. However, these catalysts reduce the use of Pt through the addition of other expensive noble metals. Therefore, a desire for research pertaining to alloying Pt with non-precious metals has arisen.

2.1.2 Platinum-Transition Metal Alloys

Zhu et al. have developed a synthesis method for the production of FePtCu nanorods (NRs) with FeCu/Pt core/shell morphology. First FePt NRs were produced via the reaction between Fe(CO)₅ and Pt(acac)₂. This was followed by the addition of a Cu salt. The resulting product was a monodispersed FePtCu alloy NR with 2x20 nm dimensions as seen in figure 9. Treatment with acetic acid and electrochemical etching in HClO₄ gave rise to the

FeCu/Pt core/shell morphology. Elemental line profiles confirmed the core/shell arrangement. Comparison of ORR activities at 0.827 V vs. RHE in 0.1 M HClO₄ showed the FeCu/Pt NRs exhibited a mass activity of ~1.034 A mg⁻¹-Pt compared to 0.138 A mg⁻¹-Pt shown by a commercial Pt/C catalyst. The improved activity exhibited can be explained most likely by the shifting of the Pt d-band that comes with a core-shell configuration [32, 33] along with the fact that the active Pt resided almost completely on the surface rather than in the core of the NRs where it is less effective as a catalyst [52].

Fig. 9. TEM image of Fe₂₉Pt₄₁Cu₃₀ NRs. Reprinted with permission from Zhu, H., et al., *Synthetic control of FePtM nanorods (M= Cu, Ni) to enhance the oxygen reduction reaction*. J Am Chem Soc, 2013. **135**(19): p. 7130-7133. Copyright 2013 American Chemical Society. [52]

Carpenter et al. have taken advantage of well faceted octahedral PtNi nano-octahedra with a predominant (111) surface for their ORR activity. Their synthesis resulted in nanoparticles ~10 nm across which can be seen via high angle annular dark field scanning transition electron microscopy (HAADF-STEM) in figure 10. As previously discussed, Stamenkovic et al. have shown the (111) face to be the most active towards ORR in an HClO₄ electrolyte. RDE studies on Carpenter's PtNi nano-octahedra support this claim. These PtNi nanoparticles outperformed a conventional Pt/C catalyst by a factor of ~4 exhibiting a mass activity of ~0.68 A mg⁻¹-Pt compared to ~0.16 A mg⁻¹-Pt at 0.9 V vs. RHE in 0.1 M HClO₄ [53].

Fig. 10. High angle annular dark field scanning transmission electron microscope (HAADF-STEM) image of PtNi nanoparticles displaying their octahedral morphology. Reprinted with permission from Carpenter, M.K., et al., *Solvothermal synthesis of platinum alloy nanoparticles for oxygen reduction electrocatalysis*. *J Am Chem Soc*, 2012. **134**(20): p. 8535-8542. Copyright 2012 American Chemical Society. [53]

Guo et al. have developed a method for the preparation of Fe₂₀Pt₈₀ nanowires with diameters of ~2.5 nm and lengths ranging from 30-100 nm as seen in figure 11. RDE tests were carried out to determine catalytic activity. The Fe₂₀Pt₈₀ nanowires exhibited a mass activity of 0.844 A mg⁻¹-Pt compared to 0.155 A mg⁻¹-Pt exhibited by a Pt/C catalyst at 0.9 V vs. RHE in 0.1 M HClO₄. Alloying the platinum with iron results in a negative shift in the d-band at the catalyst surface [54]. As proven by Kuttiyiel et al. [34] this downward shift in the d-band results in a weaker bond between the catalyst and oxygen intermediates, and this shift results in a more efficient ORR catalyst [55].

Fig. 11. TEM image of Fe₂₀Pt₈₀ nanowires on a Kethen EC-300J carbon support [55]

Choi et al. established a synthesis method for Pt_{2.5}Ni nano-octahedra. The resulting particles are monodispersed at ~9 nm across according to the TEM micrograph. This is the most active PtNi catalyst reviewed in this paper with a mass activity of ~3.3 A mg⁻¹-Pt compared to ~0.2 A mg⁻¹-Pt shown by a Pt/C catalyst at 0.9 V vs. RHE in 0.1 M HClO₄. Again, this is likely due to the predominant (111) faces exposed at the catalytic surface due to octahedral morphology [56].

Previous studies on ordered CoPt structures as ORR catalyst have shown poor activity [57], but Wang et al. have produced a Pt-on-Pt₃Co core/shell catalyst which displays impressive activity. Their synthesis resulted in a Pt rich shell ~0.5 nm thick according to elemental line profiles. RDE tests displayed in figure 12 of the Pt₃Co/Pt core/shell NPs revealed a mass activity of ~2.2 A mg⁻¹-Pt compared to ~0.25 A mg⁻¹-Pt seen by state of the art Pt/C catalyst at 0.85 V vs. RHE in 0.1 M HClO₄. The improved ORR activity of this catalyst is thought to arise from the strain put on the Pt surface via lattice mismatch; the Pt₃Co core has a smaller lattice constant than the Pt shell [58].

Fig. 12. Linear sweep voltammogram comparing Pt/C and Pt-on-Pt₃Co. Reproduced by permission from Macmillan Publishers Ltd: [Nature Materials] Wang, D., et al., *Structurally ordered intermetallic platinum–cobalt core–shell nanoparticles with enhanced activity and stability as oxygen reduction electrocatalysts*. Nature materials, 2013. **12**(1): p. 81-87, copyright 2013. [58]

Fig. 13. Comparison of power densities for Pt-TM catalysts [52, 53, 55, 56, 58]

Obviously, as seen in figure 13, alloying platinum with a transition metal drastically improves upon state of the art Pt/C catalysts in terms of ORR activity. The observed improvement in activity can be attributed to a number of factors; strain placed on a platinum skin by an underlying core with a smaller lattice constant, a shift in the d-band of the catalyst due to metal-metal interactions and morphology effects that leave the most active (111) face predominantly exposed. Indeed, the most active Pt-TM alloy in

terms of mass activity ($\text{Pt}_{2.5}\text{Ni}$ nano-octahedra made by Choi et al.) out performs the most active Pt-PM catalyst (PtPd NTs made by Alia et al.). However, with a platinum composition of about 75 at.%, these $\text{Pt}_{2.5}\text{Ni}$ catalysts do not significantly reduce platinum loading. Therefore, research into Pt-free catalysts is important and ongoing.

2.2 Platinum-Free Catalysts

All of the catalysts reviewed above improved upon the ORR performance of state of the art Pt/C catalysts, some of them significantly. However, they all incorporate platinum to some extent. With the increased Pt demand that will come with widespread PEMFC vehicle use, the Pt supply will continue to decline quite rapidly. Additionally, alloying Pt with any metal will make it more difficult to recover and recycle the Pt. One can assume that these advances will still not be enough to render PEMFC automobiles economical for mass production. Therefore, it is necessary to search for a Pt-free alternative catalyst. Because these catalysts are devoid of Pt, they will be compared on a specific activity (A cm^{-2}) basis rather than a mass activity basis.

Precious metal-free catalysts display inferior stability in acidic media compared to alkaline media [59-61]. Coupled with the fact that Pt-based catalyst display poorer activity towards the ORR and more negative onset potentials in base than in acid, it is easy to deduce the reasoning behind the following reports displaying PM-free catalytic measurements in an alkaline electrolyte [62].

2.2.1 Platinum-Free Transition Metal Based Catalysts

Liang et al. have developed a synthesis for Co_3O_4 nanocrystals (NCs) on both pure graphitic supports as well as N-doped graphitic supports. In these studies the doping of

nitrogen into a TM-C matrix improves the activity of the catalyst toward ORR. These catalysts, especially those supported on N-doped graphitic supports, show very promising current densities. RDE measurements at 0.7 V vs. RHE in 0.1 M KOH conducted with the Co₃O₄ NCs on pure carbon supports showed a current density of ~3.5 mA cm⁻², and the NCs on N-doped supports showed current densities of ~5 mA cm⁻². This is comparable to the current density seen by Pt/C catalysts under the same conditions of ~5.5 mA cm⁻². As seen in figure 15 b, the Co₃O₄ NCs on N-doped supports also showed excellent stability with little activity decay over 25,000 s compared to 20% activity loss exhibited by a state of the art platinum catalyst under the same conditions. X-ray absorption near edge structure (XANES) studies were carried out on the N-doped graphene supported NCs. The results indicated that Co-O-C and Co-N-C bonds had been formed, and that a decrease in unoccupied O 2p-Co 3d states was seen. This resulted in a higher electron density around oxygen atoms and a lower electron density around cobalt. This density shift makes the cobalt atoms attractive sites for O₂ adsorption resulting in a higher ORR activity compared to unsupported Co₃O₄ NCs [63].

Fig. 14. (a) TEM image of N-doped graphene supported Co₃O₄ NCs (b) stability test comparing N-doped graphene supported Co₃O₄ NCs and Pt/C in 0.1 M KOH. Reprinted by permission from Macmillan Publishers Ltd: [Nature Materials] Liang, Y., et al., *Co₃O₄ nanocrystals on graphene as a synergistic catalyst for oxygen reduction reaction*. Nature materials, 2011. **10**(10): p. 780-786. Copyright 2011. [63]

Liang et al. further improved upon their Co₃O₄ nanocrystals by adding manganese in a two-step solvothermal process resulting in a MnCo₂O₄/N-doped reduced graphene oxide (N-

rmGO). TEM and SEM showed a monodispersion of ~5 nm spinel crystals on N-rmGO sheets. XANES revealed that the spinel particles were covalently bound to the N-rmGO through Co-O-C and Co-N-C bonds similar to those seen in N-doped carbon supported Co_3O_4 nanocrystals [63]. The anchoring effect of these covalent bonds means that agglomeration through the life cycle is reduced, and thus the catalyst displays superior stability; it maintained peak current density for 20,000 seconds while a Pt/C catalyst saw a drop of ~30% activity under the same conditions. Tafel slope studies suggest that the ORR rate-limiting step on this catalyst is related to the protonation of oxygen once adsorbed rather than oxygen adsorption itself which is thought to limit ORR on Pt catalysts [64]. According to DFT studies carried out by Kuttiyiel et al., this implies a downward shift in the d-band compared to platinum [34]. This shift can be credited for the increased ORR activity exhibited. As displayed by figure 16 $\text{MnCo}_2\text{O}_4/\text{N-rmGO}$ displayed identical maximum current density to a Pt/C catalyst according to RDE studies displaying a specific activity of $\sim 3.8 \text{ mA cm}^{-2}$ at 0.65 V vs. RHE in 1 M KOH [65].

Fig. 15. Linear sweep voltammogram comparing Pt/C and $\text{MnCo}_2\text{O}_4/\text{N-rmGO}$. Adapted with permission from Liang, Y., et al., *Covalent hybrid of spinel manganese–cobalt oxide and graphene as advanced oxygen reduction electrocatalysts*. J Am Chem Soc, 2012. **134**(7): p. 3517-3523. Copyright 2012 American Chemical Society.

[65]

Dombrovskis et al. have successfully synthesized nitrogen activated TM ion-chelating ordered mesoporous carbon (TM-OMC) catalysts with iron and cobalt. The TM-OMC was

synthesized using a mesoporous silica template. Corresponding TM salts and furfuryl amine were used as TM and carbon/nitrogen precursors respectively. The most active catalyst tested in these studies was an iron doped (~0.9 wt%) N-functionalized OMC. Single cell PEMFC measurements shown in figure 17 display a specific activity of ~0.07 A cm⁻² for this catalyst compared to ~0.25 A cm⁻² exhibited by a state of the art Pt/C catalyst under the same conditions. These tests were carried out at 0.65 V vs. RHE. EXAFS studies show an iron oxidation state similar to that found in an iron porphyrin (Fe (II) or (III)) rather than one found in metallic iron. It is thought that the electrochemical transformation brought about by this change in oxidation state is responsible for the significant ORR activity exhibited by this catalyst [66].

Fig. 16. Single cell PEMFC studies comparing Pt/C and Fe-doped N-OMCs. Reproduced with permission from Dombrovskis, J.K., et al., *Transition metal ion-chelating ordered mesoporous carbons as noble metal-free fuel cell catalysts*. Chemistry of Materials, 2013. **25**(6): p. 856-861. Copyright 2013 American Chemical society. [66]

Deng et al have encapsulated iron nanoparticles in “pea-pod” compartments of N-doped carbon nanotubes (N-CNTs). SEM and TEM show these “pods” have graphitic walls ranging from one to eight atomic layers thick. The iron NPs themselves were fairly monodispersed at ~ 5 nm with one to two NPs per pod as seen in figure 17. Unlike Dombrovskis Fe-doped N-OMCs which displayed iron oxidation states analogous to porphyrin (Fe (II) and III), XANES reveals that the encapsulated iron shows oxidation states indicative of metallic iron (Fe (0)) [66]. Encapsulation of these NPs provided a physical

barrier between the iron and the acidic medium. The protective barrier can be credited for the good stability exhibited by these catalysts. Indeed, the Pod(N)-Fe showed a negligible drop in activity after 250 hours of testing. Pod(N)-Fe displayed a specific activity of $\sim 0.03 \text{ A cm}^{-2}$ compared to $\sim 1 \text{ A cm}^{-2}$ exhibited by a Pt/C catalyst at $\sim 0.7 \text{ V}$ vs. RHE in single cell PEMFC tests. DFT models were constructed to investigate the relatively high activity observed in Pod(N)-Fe. The results showed a charge transfer of 1.45 electrons from the iron particle to the carbon in the surrounding nanotube. The migration of electron density results in a negative free energy of oxygen adsorption facilitating ORR to take place on the catalyst surface resulting in the observed improved catalytic activity [67].

Fig. 17. TEM image of Pod(N)-Fe [67]

Hu et al. have successfully prepared hollow Fe_3C spheres surrounded by graphitic outer layers ($\text{Fe}_3\text{C}/\text{C}$). Fe_3C has exhibited promising ORR results in neutral and alkaline solutions [68, 69], but, due to its dissolution [70-72], Fe_3C 's use in acidic media has been extremely limited. However, the graphitic layers surrounding the hollow Fe_3C nanospheres act as a physical barrier between the acidic solution and the Fe_3C just as the nanotube pods protect the Fe nanoparticles in the work of Deng et al. Indeed, after 4,500 cycles between 0.6 and 1 V vs. RHE in 0.1 M HClO_4 , only negligible activity loss was observed demonstrating that the protective graphitic barrier drastically improves the stability of Fe_3C in acid. Additionally, the thin graphitic shells do not adversely affect the catalytic activity of the Fe_3C spheres. As seen in figure 19, at 0.7 V vs. RHE in 0.1 M KOH $\text{Fe}_3\text{C}/\text{C}$ displayed a current density of $\sim 4 \text{ mA cm}^{-2}$, nearly identical to the activity exhibited by Pt/C under the same conditions. [73]

Fig. 18. Linear sweep voltammogram comparing Fe₃C/C and Pt/C [73]

Fig. 19. Comparison of power densities for Pt-free TM catalysts (a) tested via RDE studies and (b) tested via single cell PEMFC assemblies [63, 65-67, 73]

The advantage of the above reviewed catalysts is obvious; they eliminate the need for expensive precious metals, and they are comparable to Pt/C in terms of activity. However, an even more ideal ORR catalyst is one that is metal free. The catalysts reviewed below represent the ideal and the true end goal of this research. Namely, inexpensive and environmentally friendly metal free PEMFC catalysts.

2.2.2 Metal-Free Catalysts

Research into metal free ORR catalysts is dominated by carbon for a few reasons: even pure amorphous carbon shows detectable activity toward ORR [74], carbon can be manipulated into various morphologies with very high surface areas [75-77], carbon materials are robust in harsh chemical environments [78], and these carbon structures display high conductivities [78-80], essential for PEMFC uses. The following section focuses on these carbon based, metal free catalysts.

As is obvious from the precious metal free TM section above, C-N sites are critical when it comes to improved catalytic activity toward ORR. Thus, carbonitrides have received much attention as ORR catalysts. However, the high concentration of nitrogen atoms found in

carbonitrides, or rather the relatively low concentration of sp² carbon atoms, decreases the conductivity of the material reducing its efficiency. Therefore, Qu et al. reduced the nitrogen content by doping graphene with nitrogen only up to 4 at %. The resultant product was an N-doped graphene which AFM data showed to be ~1 nm thick. Elemental analysis obtained from XPS studies showed the presence of both pyrrolic and pyridinic nitrogen. Catalytic testing seen in figure 21 showed that the N-graphene outperformed commercial Pt/C at 0.6 V vs. RHE in air saturated 0.1 M KOH. The N-graphene displayed a specific activity of ~0.54 mA cm⁻² compared to ~0.18 mA cm⁻² exhibited by Pt/C. Quantum mechanics calculations [81] showed that the electron withdrawing nitrogen atoms gave rise to more positively charged carbon atoms which therefore acted as ORR active sites [82].

Fig. 20. Linear sweep voltammogram comparing Pt/C and N-Graphene. Reproduced with permission from Qu, L., et al., *Nitrogen-doped graphene as efficient metal-free electrocatalyst for oxygen reduction in fuel cells*. ACS nano, 2010. 4(3): p. 1321-1326. Copyright 2010 American Chemical Society. [82]

Wohlgemuth et al. have improved upon the activity of nitrogen doped carbon by adding a second dopant, sulfur. XPS analysis showed that the sulfur-doping level, ranging from ~ 0.5 at% or ~0.7 at%, depends on the sulfur precursor used. The nitrogen doping level was consistent at ~3.4 at%. Conductivity studies comparing sulfur/nitrogen-doped aerogels (SNA's) and nitrogen-doped aerogels (NA's) showed that addition of sulfur actually increased conductivity. The sample possessing ~0.7 at% sulfur (CA_TC) showed conductivity of 660.2 S m⁻¹ compared to 503.6 S m⁻¹ exhibited by the ~0.5 at% (CA_TCA)

sample and 468.2 S m^{-1} shown by the sample with no sulfur content. CA_TCA was the most active of the synthesized catalysts towards ORR with a current density of $\sim 1.1 \text{ mA mg}^{-1}$ compared to $\sim 1 \text{ mA mg}^{-1}$ achieved by CA_TC and $\sim 0.4 \text{ mA mg}^{-1}$ shown by the NA. This was comparable to the $\sim 1.6 \text{ mA mg}^{-1}$ seen by a state of the art Pt/C catalyst in the same conditions (0.1 M KOH solution at 0.664 V vs RHE). As mentioned above, the improved ORR activity in N-doped carbon species is thought to arise from an induced dipole in C-N bonds which leaves carbon more positive and therefore more susceptible to oxygen adsorption. However, electronegativity values on the Pauling scale of carbon and sulfur are nearly identical, ruling out this theory as a reason why sulfur doping further improves ORR activity. Instead, the strain caused by the size difference between the atoms (sulfur atomic radius = 100 pm, nitrogen = 65 pm and carbon = 70 pm) [83] is thought to bring about defect sites that are responsible for the increase in activity towards ORR [84].

Fig. 21. SEM image of CA-TCA. Reproduced from [84] with permission of The Royal Society of Chemistry.

Many metal-free carbon-based ORR catalysts are produced using chemical vapor deposition (CVD) which is time consuming and expensive. However, Shuangyin Wang et al. have developed a method to produce boron and nitrogen doped carbon (BCN) by simply annealing graphite oxide (GO) in the presence of boric acid and ammonia. The composition of these catalysts is tunable allowing for (B,N) atomic percentages ranging from 13 to 72 % according to XPS. Three of these catalysts; $\text{B}_{38}\text{C}_{38}\text{N}_{34}$, $\text{B}_7\text{C}_{87}\text{N}_6$ and $\text{B}_{12}\text{C}_{77}\text{N}_{11}$ were tested for ORR activity and compared to a Pt/C catalyst. The catalyst with the highest (B,N)

content ($B_{38}C_{38}N_{34}$) showed little ORR activity. Low conductivity of this material stemming from its low carbon content is attributed for its relatively low activity. However, $B_7C_{87}N_6$ and $B_{12}C_{77}N_{11}$ both displayed promising activity values with $B_{12}C_{77}N_{11}$ being the most active of the metal free catalysts tested in this study. Indeed, at 0.7 V vs. RHE in 0.1 M KOH the activity exhibited by $B_{12}C_{77}N_{11}$ was comparable to that seen by Pt/C. $B_{12}C_{77}N_{11}$ showed a current density of $\sim 2.9 \text{ mA cm}^{-2}$ compared to $\sim 3.2 \text{ mA cm}^{-2}$ shown by Pt/C as seen in figure 22. Furthermore, rotating ring disk electrode (RRDE) experiments conducted with this catalyst show an electron transfer number near four indicating a high selectivity for full reduction. DFT calculations [81] again indicate that the electronegativity discrepancies between the three atoms give rise to more positively charged sites on the catalytic surface. These sites are then more preferred sites for oxygen adsorption, and therefore this phenomenon is credited with the high activity seen by the BCN catalysts [85].

Fig. 22. Linear sweep voltammogram comparing Pt/C and $B_{12}C_{77}N_{11}$ [85]

Shuangyin Wang et al. have also developed a method for producing vertically aligned BCN nanotubes (VA-BCN). VA-BCN preparation is achieved through the pyrolysis of just one precursor, melamine diborate, which serves as a carbon source, a boron source and a nitrogen source simultaneously. SEM and TEM images show the resulting product; an ordered and vertically aligned system of nanotubes $\sim 50 \text{ nm}$ in diameter with very few impurities. XPS analysis shows an atomic composition of 85.5:4.2:10.3 C:B:N. In theory, the high carbon content ensures that the material will possess good conductivity while the B and N atoms withdraw electrons from the carbon atoms making the carbon atoms more

positive and thus more conducive sites for ORR. As seen in figure 23 a, VA-BCN nanotubes outperformed a state of the art Pt/C catalyst in terms of specific activity at 0.7 V vs. RHE in 0.1 M KOH. The VA-BCN nanotubes exhibited an activity of $\sim 4 \text{ mA cm}^{-2}$ compared to $\sim 3 \text{ mA cm}^{-2}$ shown by Pt/C [86].

Fig. 23. (a) linear sweep voltammogram comparing VA-BCN and Pt/C (b) TEM image of VA-BCN [86]

Shubin Yang et al. have developed “sandwich-like” graphene-based CN nanosheets (G-CN) $\sim 18 \text{ nm}$ thick based on AFM. The most active catalyst from this family of materials was the one annealed at $800 \text{ }^\circ\text{C}$ (G-CN800). G-CN800 outperformed a Pt/C catalyst at 0.564 V vs. RHE in 0.1 M KOH with a current density of 7.4 mA cm^{-2} compared to 5.4 mA cm^{-2} . XPS analysis of G-CN800 revealed that this sample possessed $\sim 10 \text{ at } \%$ nitrogen. Charge transfer that results from the incorporation of nitrogen atoms [81] along with improved conductivity shown by graphitic carbon structures is thought to account for the improved ORR activity shown by G-CN800 [87].

Fig. 24. Comparison of power densities for metal free catalysts. Note: N-doped graphene was tested in an air saturated rather than O_2 saturated environment explaining the discrepancy in activity seen. The sulfur/nitrogen doped aerogels produced by Wohlgemuth et al. are not included as they were reported on a mass activity basis [82, 85-87]

2.3 Final Discussion

As was mentioned in the introduction section, ORR catalysis is a burgeoning area of research. Therefore, the catalysts reviewed above by no means represent all of the ORR research done since 2011. However, the work does provide a comprehensive review of some of the most exciting advances made in ORR catalysis in the last five years. Table 1, shown below, provides a summary of the activity and testing conditions of all of the catalysts reviewed above.

Table 1. A table displaying each catalyst reviewed and the pertinent testing conditions.

*W/mg-catalyst

The reviewed catalysts were organized into four categories: Pt-noble metal alloys, Pt-transition metal alloys, Pt-free materials and metal-free materials. In each of these categories, one or two materials represent the most promising and active catalysts. The Pt/Pd nanotubes produced by Alia et al. outperformed their counterparts in the Pt-noble metal alloy category [51], displaying activity about nine times as high as a platinum standard in the same conditions. Likewise, the Pt_{2.5}Ni nanoparticles produced by Choi et al. showed activity higher than that of the other Pt-transition metal materials. Choi et al.'s catalyst outperformed a platinum standard in the same conditions by about 16 fold [56]. Two Pt-free materials showed promising activity. The MnCO₂O₄/N-rmGO produced by Liang et al. and the Fe₃C/C produced by Hu et al. each showed activities almost equal to a platinum standard tested in the same conditions [65, 73]. Finally, the G-CN800 produced by Shubin Yang et al. exhibits activity exceeding that of a platinum standard by ~150% [87]. The activities of these premier catalysts relative to a platinum standard are displayed in figure 25 below.

Fig. 25. The highest performing catalysts from each category reviewed relative to state of the art platinum catalysts tested under the same conditions [51, 56, 65, 73, 82]

In depth cost analyses have been performed to estimate overall PEMFC costs, and figures for what kind of cost reduction needs to take place for PEMFCs to be economically competitive have been calculated in previous studies [8]. However, the research scale nature of the catalysts reviewed means that synthesis cost and scalability make it difficult to accurately estimate overall costs of the reviewed catalysts. Therefore, a convenient, and very simplified, method of cost comparison is to find the amperage per mass of metal used and divide by the cost of that metal. Of course, this method is not applicable to metal free catalysts, but the metal free nature of these materials can be used to assume a much lower cost than any metal containing material. Using this method, as well as current costs of palladium and platinum of 0.0163 \$/mg [88] and 0.0294 \$/mg respectfully [89], Alia et al.'s Pt/Pd nanotubes show a power per dollar figure of 9.73 W/\$ [51]. Using the same cost for Pt and a cost of 0.000077 \$/mg_{Ni} [90], the Pt_{2.5}Ni nanoparticles produced by Choi et al. showed a value of 99.43 W/\$ [56]. With a cost of 0.000065 \$/mg_{Mn} [91] and a cost of 0.00021 \$/mg_{Co} [92], the MnCo₂O₄ produced by Liang et al. displayed a power per dollar value of 152.5 W/\$ [65]. With the current cost of 0.000072 \$/mg_{Fe} [93], the Fe₃C catalyst produced by Hu et al. shows a value of 65.14 W/\$ [73]. Finally, with reported costs of 1 \$/mg for graphene [94], the G-CN800 catalyst produced by Shubin Yang et al. shows a meager value of 0.057 W/\$ [87]. Again, this cost analysis is dependent only on the final materials, and it does not take into account synthesis or scalability. That being said, the value based on these figures is trending toward a Pt-free material as the future of ORR catalysis.

Based on this power per dollar analysis, the obvious choice for the future of ORR catalysis is a transition metal based material. However, the cost analysis of the metal free

materials is skewed by the astronomical price of graphene (\$1/mg). As synthesis methods for graphene improve, this price will inevitably fall. This makes metal free materials seem much more viable as the future of ORR catalysis. This assumption is backed up by the recent flooding of reputable journals with articles concerning metal free, carbon based materials with applications as ORR catalysts [95-99]. Therefore, the ORR field seems to be trending toward metal-free materials. However, transition-metal based materials have shown attractive results, and the authors do not foresee a collapse of research in this field either.

3. Conclusion

Optimization of ORR catalysts is a balancing act between platinum loading and activity. The catalysts reviewed containing platinum, whether they are alloyed with precious metals or with transition metals, remain the most active as well as the most expensive. Meanwhile, Pt-free catalysts show lower ORR activity, but are much less expensive than their Pt-alloy counterparts. ORR catalysis research has followed a trend producing less and less expensive catalysts with lower and lower platinum contents. The “first generation” of research involved the activity optimization of pure platinum catalysts. The “second generation” involved preparation of Pt alloys which simultaneously increased ORR activity while decreasing platinum content. This generation is still a healthy area of research, but the time spent on these studies means that they are relatively well understood. The “third generation,” which is not as well developed as of yet, is that of precious metal free catalysts. The “fourth generation,” and the future of ORR catalysis research, is the search for metal free catalysts.

The sweet spot at the moment seems to lie in the realm of TM-containing Pt-free catalysts. Liang et al.'s $\text{MnCo}_2\text{O}_4/\text{N}$ -doped reduced graphene oxide equaled the activity of

their Pt/C counterparts under identical conditions, and showed the highest power per dollar value of 152.5 W/\$ [65]. However, the next frontier (one which is growing nearer as we speak), is the field of metal free ORR catalysts. Indeed, Qu et al. have already produced nitrogen doped graphene which outperforms Pt/C catalysts under the same conditions [82]. Due to the cost of graphene, this material is currently too expensive to be viable. However, with further optimization and scale up, affordable metal-free catalysts are on the horizon, and so are affordable fuel cell cars.

4. Acknowledgements

This research was funded by the National Science Foundation grant for the Dissemination of Nanotechnologies for Energy Production and Environment Protection in Rural Areas of Wyoming (#NSF0948027).

5. References

1. Florides, G.A. and P. Christodoulides, *Global warming and carbon dioxide through sciences*. Environment international, 2009. **35**(2): p. 390-401.
2. Irani, M., et al., *Modified nanosepiolite as an inexpensive support of tetraethylenepentamine for CO₂ sorption*. Nano Energy, 2015. **11**: p. 235-246.
3. Kong, Y., et al., *A new aerogel based CO₂ adsorbent developed using a simple sol-gel method along with supercritical drying*. Chemical Communications, 2014. **50**(81): p. 12158-12161.
4. Cui, S., et al., *Mesoporous amine-modified SiO₂ aerogel: a potential CO₂ sorbent*. Energy Environ. Sci., 2011. **4**(6): p. 2070-2074.
5. He, Y., et al., *High-efficiency conversion of CO₂ to fuel over ZnO/gC₃N₄ photocatalyst*. Applied Catalysis B: Environmental, 2015. **168**: p. 1-8.
6. He, Y., et al., *A new application of Z-scheme Ag₃PO₄/g-C₃N₄ composite in converting CO₂ to fuel*. Environmental science & technology, 2015.
7. O'Hayre, R.P., et al., *Fuel cell fundamentals*. 2006: John Wiley & Sons New York.
8. Moreno, N.G., et al., *Approaches to polymer electrolyte membrane fuel cells (PEMFCs) and their cost*. Renewable and Sustainable Energy Reviews, 2015. **52**: p. 897-906.
9. Sheng, W., H.A. Gasteiger, and Y. Shao-Horn, *Hydrogen oxidation and evolution reaction kinetics on platinum: acid vs alkaline electrolytes*. Journal of the Electrochemical Society, 2010. **157**(11): p. B1529-B1536.
10. Gasteiger, H.A. and N.M. Markovic, *Just a dream-or future reality?* Science, 2009. **324**(ANL/MSD/JA-63907).
11. Wagner, F.T., B. Lakshmanan, and M.F. Mathias, *Electrochemistry and the future of the automobile*. J. Phys. Chem. Lett, 2010. **1**(14): p. 2204-2219.

12. Appleby, A., *Electrocatalysis of aqueous dioxygen reduction*. Journal of Electroanalytical Chemistry, 1993. **357**(1): p. 117-179.
13. Stamenkovic, V.R., et al., *Improved oxygen reduction activity on Pt₃Ni (111) via increased surface site availability*. Science, 2007. **315**(5811): p. 493-497.
14. Gasteiger, H.A., et al., *Activity benchmarks and requirements for Pt, Pt-alloy, and non-Pt oxygen reduction catalysts for PEMFCs*. Applied Catalysis B: Environmental, 2005. **56**(1): p. 9-35.
15. Jaouen, F., et al., *Recent advances in non-precious metal catalysis for oxygen-reduction reaction in polymer electrolyte fuel cells*. Energy & Environmental Science, 2011. **4**(1): p. 114-130.
16. Schmidt, T., et al., *The oxygen reduction reaction on a Pt/carbon fuel cell catalyst in the presence of chloride anions*. Journal of Electroanalytical Chemistry, 2001. **508**(1): p. 41-47.
17. Hansen, H.A., V. Viswanathan, and J.K. Nørskov, *Unifying Kinetic and Thermodynamic Analysis of 2 e⁻ and 4 e⁻ Reduction of Oxygen on Metal Surfaces*. The Journal of Physical Chemistry C, 2014. **118**(13): p. 6706-6718.
18. Holton, O.T. and J.W. Stevenson, *The role of platinum in proton exchange membrane fuel cells*. Platinum Metals Review, 2013. **57**(4): p. 259-271.
19. Song, C. and J. Zhang, *Electrocatalytic oxygen reduction reaction, in PEM fuel cell electrocatalysts and catalyst layers*. 2008, Springer. p. 89-134.
20. de Morais, R.F., et al., *Coverage-Dependent Thermodynamic Analysis of the Formation of Water and Hydrogen Peroxide on Platinum Model Catalyst*. Physical Chemistry Chemical Physics, 2015.
21. Zhang, L. and Z. Xia, *Mechanisms of Oxygen Reduction Reaction on Nitrogen-Doped Graphene for Fuel Cells*. The Journal of Physical Chemistry C, 2011. **115**(22): p. 11170-11176.
22. Lim, D.-H. and J. Wilcox, *Mechanisms of the oxygen reduction reaction on defective graphene-supported Pt nanoparticles from first-principles*. The Journal of Physical Chemistry C, 2012. **116**(5): p. 3653-3660.
23. Nørskov, J.K., et al., *Origin of the overpotential for oxygen reduction at a fuel-cell cathode*. The Journal of Physical Chemistry B, 2004. **108**(46): p. 17886-17892.
24. Zhang, J., et al., *Controlling the Catalytic Activity of Platinum-Monolayer Electrocatalysts for Oxygen Reduction with Different Substrates*. Angewandte Chemie International Edition, 2005. **44**(14): p. 2132-2135.
25. Hwang, J.-J., *Sustainability study of hydrogen pathways for fuel cell vehicle applications*. Renewable and Sustainable Energy Reviews, 2013. **19**: p. 220-229.
26. Flyagina, I., et al., *DFT study of the oxygen reduction reaction on iron, cobalt and manganese macrocycle active sites*. International Journal of Hydrogen Energy, 2014. **39**(36): p. 21538-21546.
27. Knözinger, H. and K. Kochloefl, *Heterogeneous catalysis and solid catalysts*. Ullmann's Encyclopedia of Industrial Chemistry, 2002.
28. Cheng, J. and P. Hu, *Utilization of the three-dimensional volcano surface to understand the chemistry of multiphase systems in heterogeneous catalysis*. J Am Chem Soc, 2008. **130**(33): p. 10868-10869.
29. Bligaard, T., et al., *The Brønsted–Evans–Polanyi relation and the volcano curve in heterogeneous catalysis*. Journal of Catalysis, 2004. **224**(1): p. 206-217.
30. Sabatier, P., *Hydrogénations et deshydrogénations par catalyse*. Berichte der deutschen chemischen Gesellschaft, 1911. **44**(3): p. 1984-2001.
31. Christoffersen, E., et al., *Anode materials for low-temperature fuel cells: a density functional theory study*. Journal of Catalysis, 2001. **199**(1): p. 123-131.
32. Morris, A.R., M.D. Skoglund, and J.H. Holles, *Particle Size or Electronic Effect? An XAS Study of Re@ Pd Overlayer Catalysts*. Catalysis Letters. **145**(3): p. 840-850.
33. Morris, A.R., M.D. Skoglund, and J.H. Holles, *Characterization of Ni@ Pt and Co@ Pt overlayer catalysts using XAS studies*. Applied Catalysis A: General, 2015. **489**: p. 98-110.

34. Kuttiyiel, K.A., et al., *Bimetallic IrNi core platinum monolayer shell electrocatalysts for the oxygen reduction reaction*. Energy & Environmental Science, 2012. **5**(1): p. 5297-5304.
35. Zhou, K. and Y. Li, *Catalysis Based on Nanocrystals with Well-Defined Facets*. Angewandte Chemie International Edition, 2012. **51**(3): p. 602-613.
36. Wang, J.X., et al., *Oxygen reduction on well-defined core-shell nanocatalysts: particle size, facet, and Pt shell thickness effects*. J Am Chem Soc, 2009. **131**(47): p. 17298-17302.
37. Greeley, J. and J.K. Nørskov, *Combinatorial density functional theory-based screening of surface alloys for the oxygen reduction reaction*. The Journal of Physical Chemistry C, 2009. **113**(12): p. 4932-4939.
38. Yeo, K.M., et al., *Surfactant-Free Platinum-on-Gold Nanodendrites with Enhanced Catalytic Performance for Oxygen Reduction*. Angewandte Chemie International Edition, 2011. **50**(3): p. 745-748.
39. Zhang, J., et al., *Platinum monolayer on nonnoble metal-noble metal core-shell nanoparticle electrocatalysts for O₂ reduction*. The Journal of Physical Chemistry B, 2005. **109**(48): p. 22701-22704.
40. Zhang, J., et al., *Mixed-metal Pt monolayer electrocatalysts for enhanced oxygen reduction kinetics*. J Am Chem Soc, 2005. **127**(36): p. 12480-12481.
41. Xing, Y., et al., *Enhancing oxygen reduction reaction activity via Pd-Au alloy sublayer mediation of Pt monolayer electrocatalysts*. The Journal of Physical Chemistry Letters, 2010. **1**(21): p. 3238-3242.
42. Stern, M. and H. Wissenberg, *The influence of noble metal alloy additions on the electrochemical and corrosion behavior of titanium*. Journal of the Electrochemical Society, 1959. **106**(9): p. 759-764.
43. Buchanan, R., I.S. Lee, and J. Williams, *Surface modification of biomaterials through noble metal ion implantation*. Journal of biomedical materials research, 1990. **24**(3): p. 309-318.
44. Simonsen, S.B., et al., *Direct observations of oxygen-induced platinum nanoparticle ripening studied by in situ TEM*. J Am Chem Soc, 2010. **132**(23): p. 7968-7975.
45. Lim, B., et al., *Facile synthesis of highly faceted multi-octahedral Pt nanocrystals through controlled overgrowth*. Nano Lett, 2008. **8**(11): p. 4043-4047.
46. Zhang, G., et al., *One-pot synthesis of Ir@Pt nanodendrites as highly active bifunctional electrocatalysts for oxygen reduction and oxygen evolution in acidic medium*. Electrochemistry Communications, 2012. **22**: p. 145-148.
47. Lim, B., et al., *Pd-Pt bimetallic nanodendrites with high activity for oxygen reduction*. Science, 2009. **324**(5932): p. 1302-1305.
48. Karan, H.I., et al., *Catalytic activity of platinum monolayer on iridium and rhenium alloy nanoparticles for the oxygen reduction reaction*. ACS Catalysis, 2012. **2**(5): p. 817-824.
49. Shao, M., et al., *Enhanced oxygen reduction activity of platinum monolayer on gold nanoparticles*. The Journal of Physical Chemistry Letters, 2010. **2**(2): p. 67-72.
50. Lima, F., et al., *Catalytic activity-d-band center correlation for the O₂ reduction reaction on platinum in alkaline solutions*. The Journal of Physical Chemistry C, 2007. **111**(1): p. 404-410.
51. Alia, S.M., et al., *Platinum-coated palladium nanotubes as oxygen reduction reaction electrocatalysts*. ACS Catalysis, 2012. **2**(5): p. 858-863.
52. Zhu, H., et al., *Synthetic control of FePtM nanorods (M= Cu, Ni) to enhance the oxygen reduction reaction*. J Am Chem Soc, 2013. **135**(19): p. 7130-7133.
53. Carpenter, M.K., et al., *Solvothermal synthesis of platinum alloy nanoparticles for oxygen reduction electrocatalysis*. J Am Chem Soc, 2012. **134**(20): p. 8535-8542.
54. Gan, L., et al., *Core-Shell Compositional Fine Structures of Dealloyed Pt_xNi_{1-x} Nanoparticles and Their Impact on Oxygen Reduction Catalysis*. Nano Lett, 2012. **12**(10): p. 5423-5430.

55. Guo, S., et al., *FePt and CoPt nanowires as efficient catalysts for the oxygen reduction reaction*. *Angewandte Chemie International Edition*, 2013. **52**(12): p. 3465-3468.
56. Choi, S.I., et al., *Synthesis and characterization of 9 nm Pt-Ni octahedra with a record high activity of 3.3 A/mg(Pt) for the oxygen reduction reaction*. *Nano Lett*, 2013. **13**(7): p. 3420-5.
57. Watanabe, M., et al., *Activity and Stability of Ordered and Disordered Co-Pt Alloys for Phosphoric Acid Fuel Cells*. *Journal of the Electrochemical Society*, 1994. **141**(10): p. 2659-2668.
58. Wang, D., et al., *Structurally ordered intermetallic platinum-cobalt core-shell nanoparticles with enhanced activity and stability as oxygen reduction electrocatalysts*. *Nature materials*, 2013. **12**(1): p. 81-87.
59. Popov, B.N., et al., *Power source research at USC: Development of advanced electrocatalysts for polymer electrolyte membrane fuel cells*. *International Journal of Hydrogen Energy*, 2011. **36**(2): p. 1794-1802.
60. Liu, G., et al., *Development of non-precious metal oxygen-reduction catalysts for PEM fuel cells based on N-doped ordered porous carbon*. *Applied Catalysis B: Environmental*, 2009. **93**(1): p. 156-165.
61. Liu, G., et al., *Studies of oxygen reduction reaction active sites and stability of nitrogen-modified carbon composite catalysts for PEM fuel cells*. *Electrochimica Acta*, 2010. **55**(8): p. 2853-2858.
62. Perez, J., E. Gonzalez, and E. Ticianelli, *Oxygen electrocatalysis on thin porous coating rotating platinum electrodes*. *Electrochimica Acta*, 1998. **44**(8): p. 1329-1339.
63. Liang, Y., et al., *Co₃O₄ nanocrystals on graphene as a synergistic catalyst for oxygen reduction reaction*. *Nature materials*, 2011. **10**(10): p. 780-786.
64. Hsueh, K.L., et al., *Effects of phosphoric acid concentration on oxygen reduction kinetics at platinum*. *Journal of the Electrochemical Society*, 1984. **131**(4): p. 823-828.
65. Liang, Y., et al., *Covalent hybrid of spinel manganese-cobalt oxide and graphene as advanced oxygen reduction electrocatalysts*. *J Am Chem Soc*, 2012. **134**(7): p. 3517-3523.
66. Dombrovskis, J.K., et al., *Transition metal ion-chelating ordered mesoporous carbons as noble metal-free fuel cell catalysts*. *Chemistry of Materials*, 2013. **25**(6): p. 856-861.
67. Deng, D., et al., *Iron Encapsulated within Pod-like Carbon Nanotubes for Oxygen Reduction Reaction*. *Angewandte Chemie International Edition*, 2013. **52**(1): p. 371-375.
68. Wen, Z., et al., *Nitrogen-Enriched Core-Shell Structured Fe/Fe₃C-C Nanorods as Advanced Electrocatalysts for Oxygen Reduction Reaction*. *Advanced Materials*, 2012. **24**(11): p. 1399-1404.
69. Lee, J.S., et al., *A Highly Efficient Electrocatalyst for the Oxygen Reduction Reaction: N-Doped Ketjenblack Incorporated into Fe/Fe₃C-Functionalized Melamine Foam*. *Angew Chem Int Ed Engl*, 2013. **125**(3): p. 1060-1064.
70. Liao, Y., et al., *Facile synthesis of high-crystallinity graphitic carbon/Fe₃C nanocomposites as counter electrodes for high-efficiency dye-sensitized solar cells*. *ACS applied materials & interfaces*, 2013. **5**(9): p. 3663-3670.
71. Easton, E.B., et al., *Magnetron sputtered Fe-C-N, Fe-C, and C-N based oxygen reduction electrocatalysts*. *Journal of the Electrochemical Society*, 2008. **155**(6): p. B547-B557.
72. Giordano, C., et al., *Non-conventional Fe₃C-based nanostructures*. *Journal of Materials Chemistry*, 2011. **21**(42): p. 16963-16967.
73. Hu, Y., et al., *Hollow Spheres of Iron Carbide Nanoparticles Encased in Graphitic Layers as Oxygen Reduction Catalysts*. *Angewandte Chemie International Edition*, 2014. **53**(14): p. 3675-3679.
74. Wu, G., et al., *High-performance electrocatalysts for oxygen reduction derived from polyaniline, iron, and cobalt*. *Science*, 2011. **332**(6028): p. 443-447.

75. Yang, Z., Y. Xia, and R. Mokaya, *Enhanced hydrogen storage capacity of high surface area zeolite-like carbon materials*. *J Am Chem Soc*, 2007. **129**(6): p. 1673-1679.
76. Saliger, R., et al., *High surface area carbon aerogels for supercapacitors*. *Journal of Non-Crystalline Solids*, 1998. **225**: p. 81-85.
77. Xu, B., et al., *Highly mesoporous and high surface area carbon: a high capacitance electrode material for EDLCs with various electrolytes*. *Electrochemistry Communications*, 2008. **10**(5): p. 795-797.
78. Balandin, A.A., et al., *Superior thermal conductivity of single-layer graphene*. *Nano Lett*, 2008. **8**(3): p. 902-907.
79. Pei, S., et al., *Direct reduction of graphene oxide films into highly conductive and flexible graphene films by hydrohalic acids*. *Carbon*, 2010. **48**(15): p. 4466-4474.
80. Cai, D., M. Song, and C. Xu, *Highly Conductive Carbon-Nanotube/Graphite-Oxide Hybrid Films*. *Advanced Materials*, 2008. **20**(9): p. 1706-1709.
81. Gong, K., et al., *Nitrogen-doped carbon nanotube arrays with high electrocatalytic activity for oxygen reduction*. *Science*, 2009. **323**(5915): p. 760-764.
82. Qu, L., et al., *Nitrogen-doped graphene as efficient metal-free electrocatalyst for oxygen reduction in fuel cells*. *ACS nano*, 2010. **4**(3): p. 1321-1326.
83. Slater, J.C., *Atomic radii in crystals*. *The Journal of Chemical Physics*, 1964. **41**(10): p. 3199-3204.
84. Wohlgemuth, S.-A., et al., *A one-pot hydrothermal synthesis of sulfur and nitrogen doped carbon aerogels with enhanced electrocatalytic activity in the oxygen reduction reaction*. *Green Chemistry*, 2012. **14**(5): p. 1515-1523.
85. Wang, S., et al., *BCN Graphene as Efficient Metal-Free Electrocatalyst for the Oxygen Reduction Reaction*. *Angewandte Chemie International Edition*, 2012. **51**(17): p. 4209-4212.
86. Wang, S., et al., *Vertically Aligned BCN Nanotubes as Efficient Metal-Free Electrocatalysts for the Oxygen Reduction Reaction: A Synergetic Effect by Co-Doping with Boron and Nitrogen*. *Angewandte Chemie International Edition*, 2011. **50**(49): p. 11756-11760.
87. Yang, S., et al., *Graphene-Based Carbon Nitride Nanosheets as Efficient Metal-Free Electrocatalysts for Oxygen Reduction Reactions*. *Angewandte Chemie International Edition*, 2011. **50**(23): p. 5339-5343.
88. *Palladium Prices*. 2016 February 12, 2016 [cited 2016 February 12]; Available from: <http://www.apmex.com/spotprices/palladium-price>.
89. *Platinum Prices*. 2016 February 12, 2016 [cited 2016 February 12]; Available from: <http://www.apmex.com/spotprices/platinum-price>.
90. *Nickel*. [cited 2016 February 12]; Available from: <http://www.chemicool.com/elements/nickel.html>.
91. *Manganese*. [cited 2016 February 12]; Available from: <http://www.chemicool.com/elements/manganese.html>.
92. *Cobalt*. [cited 2016 February 12]; Available from: <http://www.chemicool.com/elements/cobalt.html>.
93. *Iron*. [cited 2016 February 12]; Available from: <http://www.chemicool.com/elements/iron.html>.
94. Konrad, T. *Investors See Great Potential In Graphene*. [cited 2016 February 12]; Available from: <http://www.forbes.com/sites/tomkonrad/2013/09/24/investors-see-great-potential-in-graphene/#21bc5d4b2077>.
95. Ma, Z., et al., *Sulfur-Doped Graphene Derived from Cycled Lithium–Sulfur Batteries as a Metal-Free Electrocatalyst for the Oxygen Reduction Reaction*. *Angewandte Chemie International Edition*, 2015. **54**(6): p. 1888-1892.
96. Gong, Y., et al., *Boron-and nitrogen-substituted graphene nanoribbons as efficient catalysts for oxygen reduction reaction*. *Chemistry of Materials*, 2015. **27**(4): p. 1181-1186.

97. Gao, S., et al., *Transforming organic-rich amaranthus waste into nitrogen-doped carbon with superior performance of the oxygen reduction reaction*. Energy & Environmental Science, 2015. **8**(1): p. 221-229.
98. Wan, K., et al., *Nitrogen-doped ordered mesoporous carbon: synthesis and active sites for electrocatalysis of oxygen reduction reaction*. Applied Catalysis B: Environmental, 2015. **165**: p. 566-571.
99. Ferrero, G., et al., *The influence of pore size distribution on the oxygen reduction reaction performance in nitrogen doped carbon microspheres*. Journal of Materials Chemistry A, 2016.
100. Bligaard, T., et al., *The Brønsted–Evans–Polanyi relation and the volcano curve in heterogeneous catalysis*. Journal of Catalysis, 2004. **224**(1): p. 206-217.

Figure Captions

Fig. 1. Mechanism schematics based on the work of Zhang et al. [24] of (a) full reduction and (b) partial reduction of oxygen

Fig. 2. Volcano plot showing relationship between oxygen binding energy and maximal activity calculated using Sabatier Analysis [23, 100]

Fig. 3. (a) TEM image of Pt/Ir nanodendrites (b) linear sweep voltammogram comparing ORR activity of Pt/Ir nanodendrites and Ir-Pt mixture [46]

Fig. 4. Linear sweep voltammogram comparing Pt/Au nanodendrites and platinum black [38]

Fig. 5. Volcano plot displaying calculated OH binding energy vs. experimentally measured current density [48]

Fig. 6. (a) plot comparing d-band center and oxygen binding energy (b) plot of current density vs. oxygen binding energy [34]

Fig. 7. (a) TEM image of PtPd14 (b) SEM image of PtPd14[51]

Fig. 8. Comparison of power densities for Pt/PM alloy catalysts [34, 38, 46, 48, 49, 51]

Fig. 9. TEM image of $\text{Fe}_{29}\text{Pt}_{41}\text{Cu}_{30}$ NRs [52]

Fig. 10. High angle annular dark field scanning transmission electron microscope (HAADF-STEM) image of PtNi nanoparticles displaying their octahedral morphology [53]

Fig. 11. TEM image of $\text{Fe}_{20}\text{Pt}_{80}$ nanowires on a Kethen EC-300J carbon support [55]

Fig. 12. Linear sweep voltammogram comparing Pt/C and Pt-on- Pt_3Co [58]

Fig. 13. Comparison of power densities for Pt-TM catalysts [52, 53, 55, 56, 58]

Fig. 14. (a) TEM image of N-doped graphene supported Co_3O_4 NCs (b) stability test comparing N-doped graphene supported Co_3O_4 NCs and Pt/C in 0.1 M KOH [63]

Fig. 15. Linear sweep voltammogram comparing Pt/C and $\text{MnCo}_2\text{O}_4/\text{N-rmGO}$ [65]

Fig. 16. Single cell PEMFC studies comparing Pt/C and Fe-doped N-OMCs [66]

Fig. 17. TEM image of $\text{Pd}(\text{N})\text{-Fe}$ [67]

Fig. 18. Linear sweep voltammogram comparing $\text{Fe}_3\text{C}/\text{C}$ and Pt/C [73]

Fig. 19. Comparison of power densities for Pt-free TM catalysts (a) tested via RDE studies and (b) tested via single cell PEMFC assemblies [63, 65-67, 73]

Fig. 20. Linear sweep voltammogram comparing Pt/C and N-Graphene [82]

Fig. 21. SEM image of CA-TCA [84]

Fig. 22. Linear sweep voltammogram comparing Pt/C and B₁₂C₇₇N₁₁ [85]

Fig. 23. (a) linear sweep voltammogram comparing VA-BCN and Pt/C (b) TEM image of VA-BCN [86]

Fig. 24. Comparison of power densities for metal free catalysts. Note: N-doped graphene was tested in an air saturated rather than O₂ saturated environment explaining the discrepancy in activity seen. The sulfur/nitrogen doped aerogels produced by Wohlgemuth et al. are not included as they were reported on a mass activity basis [82, 85-87]

Table 1. A table displaying each catalyst reviewed and the pertinent testing variables.

*W/mg-catalyst

Fig. 25. The highest performing catalysts from each category reviewed relative to state of the art platinum catalysts tested under the same conditions [51, 56, 65, 73, 82]

